Article

rGO Functionalized ZnO–TiO$_2$ Core-Shell Flower-Like Architectures for Visible Light Photocatalysis

Evangelia Vasilaki [1,2,3,*], Nikos Katsarakis [1,3], Spyros Dokianakis [1] and Maria Vamvakaki [2,3]

1   Center of Materials Technology and Photonics, Hellenic Mediterranean University,
    714 10 Heraklion, Crete, Greece; katsan@hmu.gr (N.K.); sdokianakis@hmu.gr (S.D.)
2   Department of Materials Science and Technology, University of Crete, 700 13 Heraklion, Crete, Greece;
    vamvakak@materials.uoc.gr
3   Institute of Electronic Structure and Laser, Foundation for Research & Technology-Hellas,
    700 13 Heraklion, Crete, Greece
*   Correspondence: evasilaki@iesl.forth.gr; Tel.: +30-2810545047

Abstract: Core-shell heterostructures with a complex, flower-like morphology, comprising a ZnO core and a TiO$_2$ shell decorated with reduced graphene oxide (rGO) sheets by hydrothermal wrapping, are reported to extend the absorption properties of the semiconductors toward the visible light range. The ternary photocatalysts were characterized by X-ray diffraction, field emission scanning electron microscopy, Raman spectroscopy, diffuse reflectance UV–Vis, and attenuated total reflectance-Fourier transform infrared spectroscopy. Its photocatalytic performance was evaluated under visible light irradiation using methylene blue dye as a model pollutant. The rGO-modified ZnO–TiO$_2$ photocatalyst exhibited superior photoactivity compared to that of the parent ZnO–TiO$_2$ core-shell structures, which was dependent on its graphene content. The enhanced photocatalytic response was attributed to the higher absorption in the visible light range, as well as the pronounced electron and hole separation in the ternary system.

Keywords: titanium dioxide; zinc oxide; photocatalysis; hybrid materials; reduced graphene oxide; complex architectures

1. Introduction

The intense industrialization of the last decades has resulted in the continuous introduction of industrial and agro-industrial wastewaters in aqueous matrices; heterogeneous photocatalysis has been proposed as an efficient alternative to conventional methods for their effective treatment. TiO$_2$ has been the most widely used photocatalyst, but the maximization of its photocatalytic response is hindered by its inadequate absorption in the visible light range, as well as the high degree of recombination of the photogenerated charge carrier pairs. The synthesis of core-shell heterostructures comprising TiO$_2$ and ZnO has been evaluated as an effective approach to diminish charge recombination due to the favorable energy differences between the two semiconductors [1–5]. The modification of TiO$_2$ or ZnO with reduced graphene oxide (rGO) sheets has been shown to present synergistic advantages such as a suppressed recombination of the photogenerated charge carriers and the extension of the photoresponse toward the visible light range [6–11].

The preparation of ternary photocatalysts, comprising TiO$_2$, ZnO and rGO, has been scarcely studied. Previous reports on ternary TiO$_2$, ZnO, and rGO photocatalysts focused on the nanocomposites of mixed inorganic particles prepared by conventional sol-gel, hydrothermal methods, or other modern synthetic approaches such as sonochemistry or microwave treatment [12–20]. In an important study, Johra et al. synthesized a mixed photocatalyst comprising TiO$_2$ and ZnO particles that were surface-modified with graphene oxide (GO) via a hydrothermal reaction [12]. The mixed photocatalyst exhibited increased

photocatalytic performance in the UV degradation of Cr(VI) compared with the parent TiO_2–ZnO analogues that were assigned to enhance light absorption and better the separation of electron-hole pairs. Potle et al. also compared the preparation of a mixed photocatalyst, based on TiO_2 and ZnO modified by rGO, via conventional stirring and a sonochemical approach. The application of ultrasound suppressed the aggregation of the inorganic nanoparticles and resulted in a better dispersion on the rGO sheets, which was reflected by more effective photocatalytic activity [13]. Simsek et al. immobilized rGO sheets on fluorine-doped tin oxide (FTO) substrates, followed by the hydrothermal growth of ZnO and TiO_2 nanoparticles on graphene sheets. They observed a band-gap narrowing for the ternary photocatalyst and superior photocatalytic performance against estrogen bisphenol-A and pharmaceuticals under UV and visible-light irradiation.

Architectures of a higher complexity have not been examined, yet it is known that the morphology of the ZnO–TiO_2 heterostructures heavily affects significant properties of the composite material such as the surface area and the contact between the two interfaces; thus, its control is important [21]. The contact between the rGO sheets and the inorganic component has been reported to significantly influence the photocatalytic performance of the composite photocatalyst; however, the degree of contact in the ternary photocatalysts presented so far is rather poor [22–25]. Therefore, the tailored synthesis of rGO functionalized ZnO–TiO_2 core-shell heterostructures with a complex and well-defined morphology, as well as a visible light photocatalytic activity, is expected to attract great scientific interest and will find wide applicability in wastewater treatment.

In the present work, we report the development of complex ZnO–TiO_2 core-shell, flower-like heterostructures and the extension of its photocatalytic response toward the visible light range via wrapping the inorganic surface with rGO sheets. First, well-defined core-shell, flower-like architectures, with a wurtzite ZnO core and an anatase TiO_2 shell, were synthesized by controlled sol-gel reactions. Next, the ZnO–TiO_2 heterostructures were surface-functionalized with 3-aminopropyltrimethoxysilane (APTMS) and hydrothermally wrapped with rGO sheets at tunable mass ratios, resulting in a strong rGO–inorganic surface contact. The photocatalytic performance of the obtained rGO–ZnO–TiO_2 ternary photocatalysts was evaluated in the decoloration of aqueous solutions of methylene blue (MB) under visible light irradiation.

2. Results and Discussion

2.1. Graphene Oxide

The GO was synthesized by a modified Hummers' method using graphite powder [26] and was characterized by XRD and Raman spectroscopy, and FTIR (Figure 1). A single peak at ~10° can be observed in the XRD pattern of the GO (Figure 1a), which can be assigned to the (001) crystalline plane of the GO, verifying the successful oxidation of graphite [27–29].
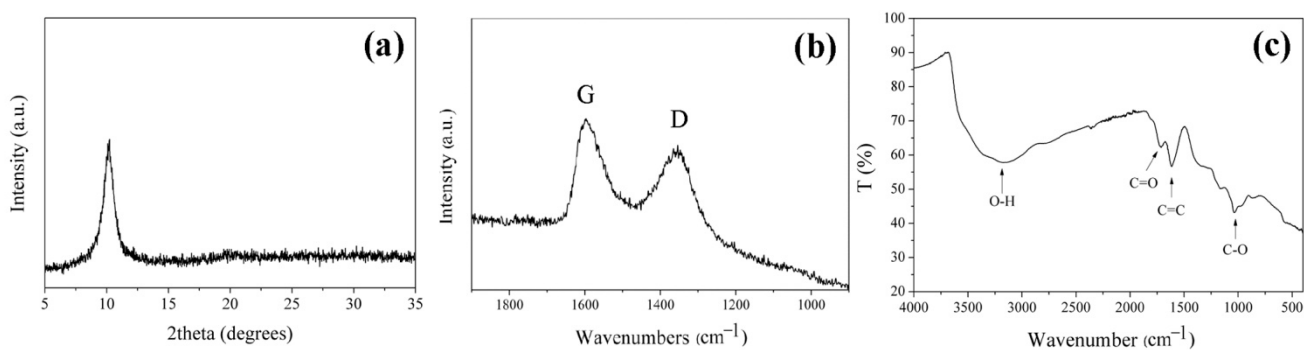
Figure 1. (**a**) XRD pattern, (**b**) Raman, and (**c**) FTIR spectra of graphene oxide (GO).

The Raman spectrum of the GO (Figure 1b) exhibited peaks at ~1355 and 1600 cm^{-1}, assigned to the typical D and G bands of graphitic materials, respectively [30,31]. Specifi-

cally, the D band can be attributed to the modes of the sp^2 atoms in the rings, while the G band is due to the stretching vibration of the sp^2-hybridized C–C bonds [32].

The ATR-FTIR spectrum of the GO presented in Figure 1c shows typical peaks associated with the oxygen functionalities introduced onto the rGO sheets upon the oxidation of graphite. In particular, the broad band at ~3400 cm^{-1} can be assigned to O–H stretching vibration, while the peaks at ~1720 and 1040 cm^{-1} are ascribed to C=O and C–O stretching vibrations, respectively. Moreover, the peak at 1615 cm^{-1} is derived from the vibrations of the remaining unoxidized graphitic domains [33,34].

2.2. ZnO Flower-Like Structures and ZnO–TiO$_2$ Core-Shell Heterostructures

The SEM and TEM images of the ZnO and the ZnO–TiO$_2$ core-shell architectures are shown in Figure 2. Well-defined flower-like ZnO structures with a smooth surface (Figure 2a,c and Figure S1a) were observed. After coating with a TiO$_2$ shell, non-agglomerated core-shell structures were obtained with a uniform porous titania shell of 59 ± 7 nm thickness (Figure 2b,d and Figure S1b). Based on the findings of our previous work, where the photoactivity of ZnO–TiO$_2$ core-shell, flower-like architectures with variable titania shell thickness were evaluated, a shell thickness of ~59 nm was found to exhibit the highest photocatalytic performance [2].
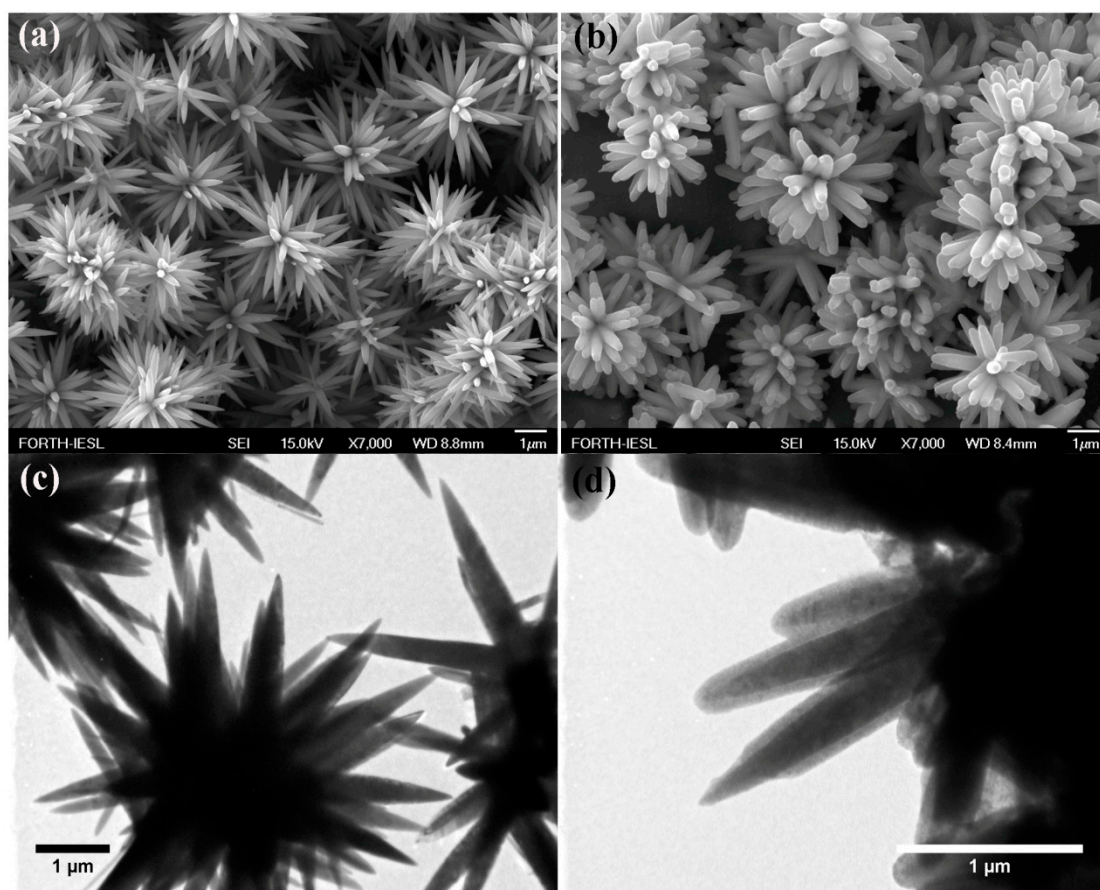
Figure 2. (**a**,**b**) SEM and (**c**,**d**) TEM images of the ZnO flower-like structures (**a**,**c**) and the ZnO–TiO$_2$ core-shell heterostructures (**b**,**d**).

2.3. rGO-Modified ZnO–TiO$_2$ Core-Shell Heterostructures

To investigate the effect of APTMS pre-treatment on the morphology of the ternary photocatalysts, the synthesis of rGO-modified ZnO–TiO$_2$ structures (denoted as ZT-rGO) was first carried out using ZnO–TiO$_2$ heterostructures with and without amine functionalization. As shown in Figure 3, when the surface of the ZnO–TiO$_2$ flower-like structures

were not amine-functionalized before the introduction of the GO at a 2 wt % content, the rGO sheets did not wrap the inorganic material well (indicated by the white arrow in Figure 3a). On the contrary, the amine pre-functionalized flower-like structures were completely wrapped with the rGO sheets, which attached very well onto the inorganic surface (Figure 3b).
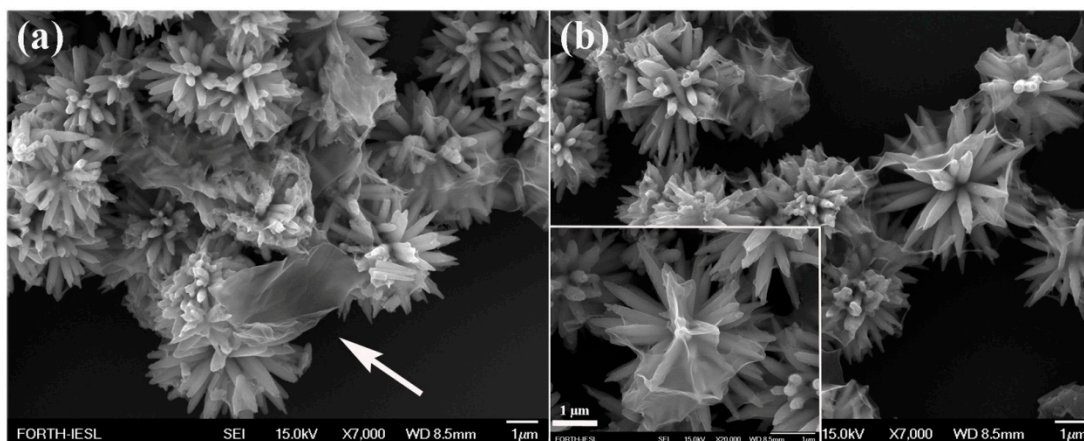
Figure 3. SEM images of rGO-modified ZnO–TiO$_2$ structures (ZT-rGO) structures at a 2 wt % reduced GO (rGO) loading without (**a**) and with (**b**) 3-aminopropyltrimethoxysilane (APTMS) functionalization.

The observed increase in the adhesion of the rGO sheets onto the surface of the ZnO–TiO$_2$ heterostructures can be assigned to the favorable electrostatic interactions between the amine-modified inorganic surface and the rGO sheets. The APTMS functionalization of the ZnO–TiO$_2$ core-shell, flower-like heterostructures resulted in the formation of a positively charged inorganic surface onto which the negatively charged rGO sheets could readily attach [34–38]. The high contact degree between the rGO layers and the semiconductor resulted in an effective charge separation during the photocatalytic process, which is highly desirable [22–25]. Therefore, the APTMS functionalized ZnO–TiO$_2$ core-shell, flower-like structures were employed in all the experiments discussed below.

The rGO sheets were attached onto the APTMS-modified ZnO–TiO$_2$ core-shell, flower-like structures at different GO loadings. The obtained ternary catalyst structures are shown in Figure 4. The attachment of the rGO sheets on the flower-like structures was heavily affected by the rGO content of the composite. The rGO sheets completely wrapped the inorganic structures at 0.5 and 2 wt % graphitic loading (Figure 4a,b and Figure S1c); above this plateau value (Figure 4c), unattached rGO sheets (indicated by white arrows) were also observed.

The rGO-modified core-shell semiconductors were characterized by ATR-FTIR (Figure 4d). The spectra of the ZT-rGO structures exhibited new peaks at ~1560 and 1230 cm^{-1}, which were attributed to the C=C skeletal vibration mode and C–O–C stretching vibration of rGO, respectively [39,40]. The peak at 1400 cm^{-1} can be attributed to the C–OH vibration mode of the graphitic material. As expected, the intensity of the peaks decreased with the reduction in the rGO loading.

Raman spectroscopy was also employed to verify the wrapping of the rGO sheets on the surface of the ZnO–TiO$_2$ core-shell, flower-like structures (Figure 5). The peaks at 142, 391, 517, and 630 cm^{-1} observed for TiO$_2$ can be attributed to the Eg, B$_{1g}$, A$_{1g}$ + B$_{1g}$, and E$_g$ modes of the anatase phase, respectively [41]. Two peaks of low intensity can be observed in the Raman spectrum of the ZnO flowers at 435 and 1145 cm^{-1}, corresponding to the E$_2^{high}$ and 2LO modes of wurtzite ZnO [42–44]. The peaks were also detected in the spectrum of the ZnO–TiO$_2$ core-shell, flower-like structures (Figure 5a), whereas the ZT-rGO ternary material exhibited two additional Raman lines at 1355 and 1590 cm^{-1}, attributed to the D and G peaks of rGO, respectively.
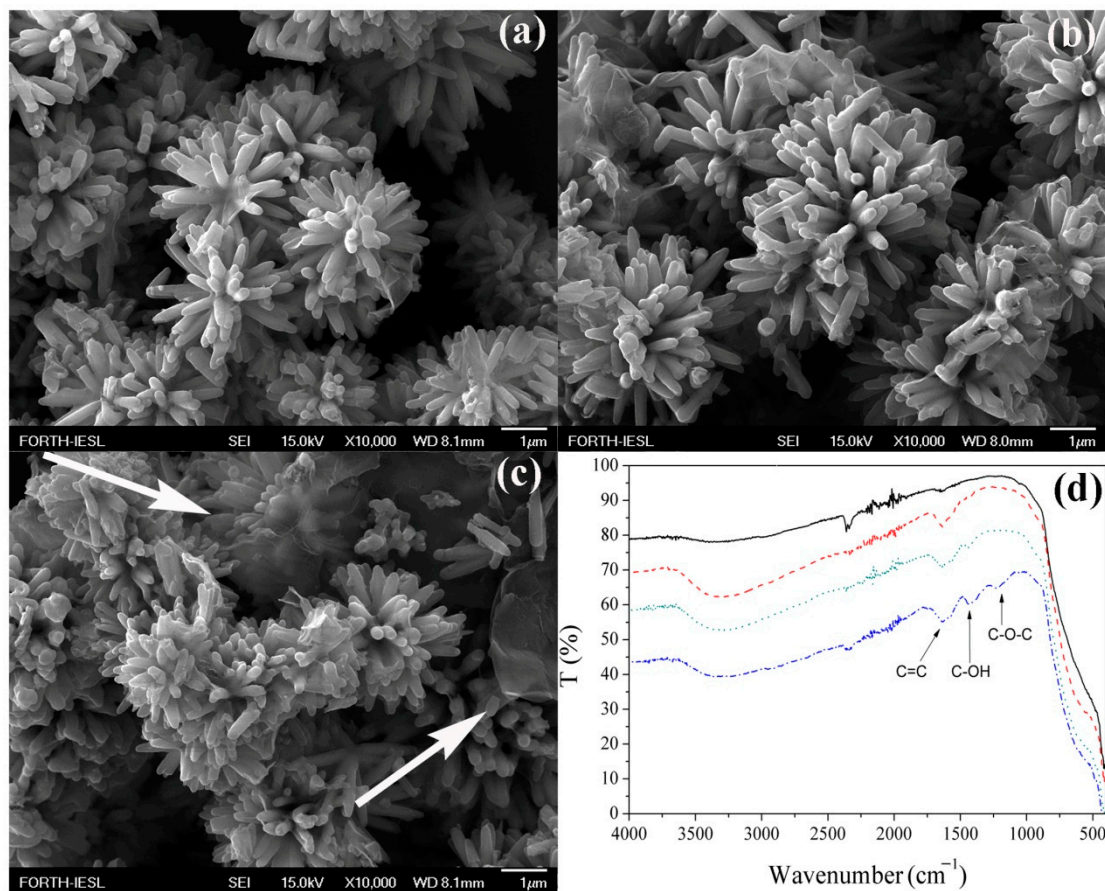
Figure 4. SEM images of ZT-rGO with (**a**) 0.5, (**b**) 2, and (**c**) 5 wt % rGO content; (**d**) ATR-FTIR spectra of the parent ZnO-TiO$_2$ core-shell flowers (black line, solid) and ZT-rGO at 0.5 (red line, dash), 2 green line, dot), and 5 wt % (blue line, dash dot) rGO loading. The white arrows indicate unattached rGO sheets.
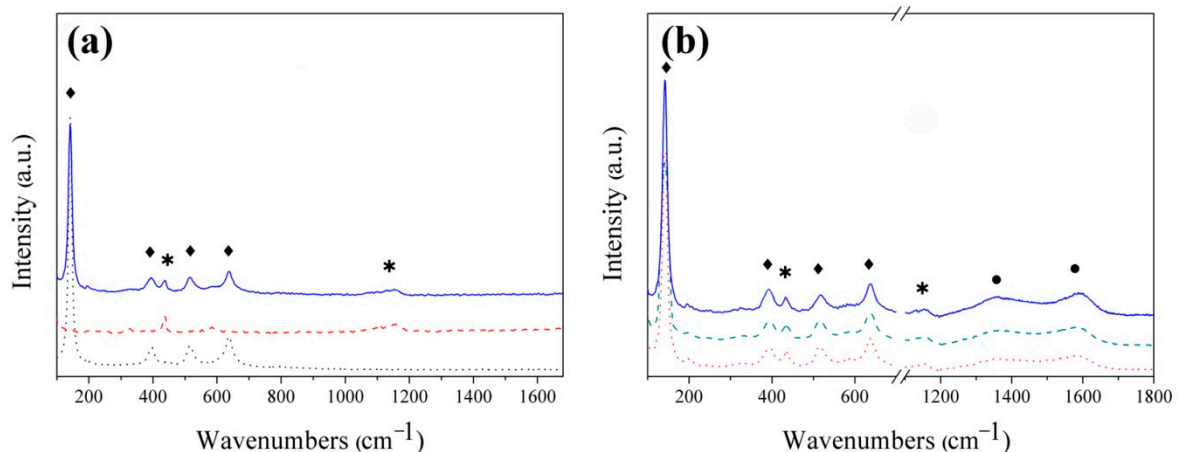
Figure 5. Raman spectra of (**a**) anatase TiO$_2$ (black dotted line), the wurtzite ZnO flowers (red dashed line), and the ZnO-TiO$_2$ core-shell flowers (blue solid line) and (**b**) ZT-rGO with 0.5 (red dotted line), 2 (green dashed line), and 5 wt % (blue solid line) rGO (the TiO$_2$ peaks are indicated with a rhombus, the ZnO peaks with an asterisk and the rGO peaks with a circle).

The band gap energy values (E$_g$) of the synthesized ZT-rGO materials were quantified by UV–Vis diffuse reflectance measurements, employing the Tauc equation:

$$\alpha h\nu = A(h\nu - Eg)^{1/n} \tag{1}$$

where hν is the photon energy, A is an energy-independent constant, and n = 2, as the indirect band gap, TiO_2 is the outer material in the core-shell heterostructures [1].

The normalized and transformed Kubelka–Munk plots as a function of light energy are shown in Figure 6, while the calculated E_g values are presented in Table 1. A narrowing in the band-gap values and a redshift in the absorbance edge were observed in the ZT-rGO structures compared with their parent ZnO–TiO_2 analogue, in agreement with the literature [45–47]. An E_g of 3.08 eV was calculated for the ZnO–TiO_2 heterostructures, lower than the values reported for the bare ZnO and TiO_2 (~3.2–3.3 eV) nanoparticles [2]. This phenomenon can be assigned to the generation of new energy states at the ZnO and TiO_2 heterojunction [48]. The E_g values of the ternary photocatalysts decreased monotonically with the increase in the rGO content due to the generation of Ti–O–C bonds during the thermal treatment, as we reported in our earlier work [6].
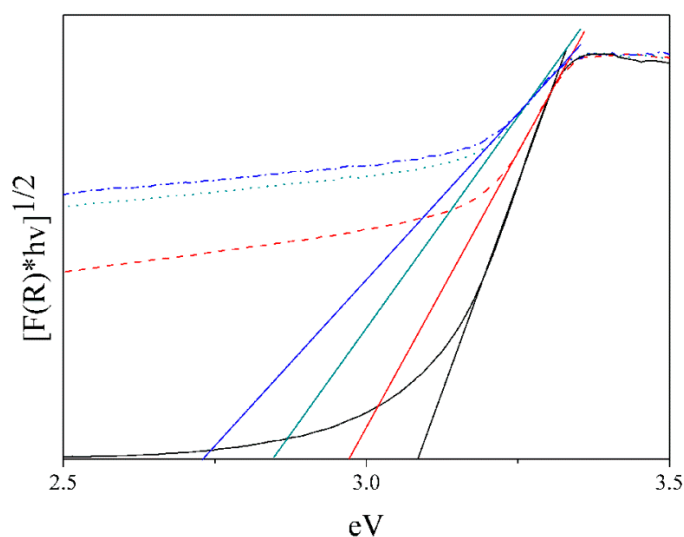
Figure 6. Normalized and transformed Kubelka–Munk function versus the light energy for the parent ZnO-TiO_2 core-shell flowers (black line, solid) and ZT-rGO at 0.5 (red line, dash), 2 (green line, dot), and 5 wt % (blue line, dash dot) rGO loading.

Table 1. Calculated optical band-gap values (E_g) for the ZnO–TiO_2 and the ZT-rGO core-shell structures.

Sample	E_g (eV)
ZnO–TiO_2	3.08
ZT-rGO 0.5 wt %	2.97
ZT-rGO 2 wt %	2.84
ZT-rGO 5 wt %	2.72

Next, the photoactivity of the parent core-shell and the ZT-rGO structures was investigated in the decoloration of aqueous MB solutions under visible-light irradiation (Figure 7).
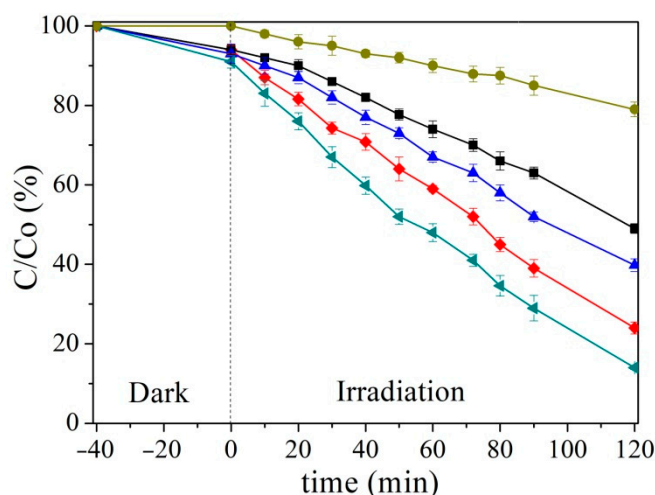
Figure 7. Decoloration of methylene blue (MB) in the absence of a photocatalyst (●) and in the presence of parent ZnO–TiO$_2$ core-shell flowers (■) and ZT-rGO at 0.5 (◆), 2 (◄), and 5 wt % (▲) rGO.

The kinetic rate constants, k, for the decoloration process of MB were calculated from the first-order equation:

$$\ln \frac{C}{Co} = -kt \tag{2}$$

The regression coefficient of the linear fits, R^2, was greater than 0.99 for all studied samples.

The photocatalytic activity of the rGO-modified ZnO–TiO$_2$ core-shell, flower-like photocatalysts was, for all studied samples, superior compared to that of the parent ZnO–TiO$_2$ core-shell semiconductor. A graphitic-content-dependent performance was observed, which was optimum for the ZT-rGO sample with 2 wt % rGO loading, and was reduced upon further increase in the rGO loading to 5 wt %.

The parent ZnO–TiO$_2$ photocatalyst exhibited a ~51% dye decoloration (rate constant k = 0.0056 min^{-1}) after a 120 min irradiation time. The decrease in the dye concentration for the ZT-rGO sample with 0.5 wt % rGO was 76% (k = 0.011 min^{-1}), while the ZT-rGO photocatalyst with 2 wt % rGO exhibited the highest photocatalytic performance with an 86% dye removal (k = 0.015 min^{-1}). Lastly, upon increasing the rGO loading to 5 wt % a decrease in the performance of the ZT-rGO photocatalyst to a 60% dye decoloration, with a rate constant k = 0.007 min^{-1}, was found.

The reusability of the ZT-rGO catalyst with 2 wt % rGO, which exhibited the highest photocatalytic activity, was evaluated for three photocatalytic cycles. As shown in Figure 8, the photocatalyst exhibited excellent reusability, with its performance decreasing only by ~8% after three photocatalytic cycles. This is indirect evidence that the intimate contact between the inorganic component and the rGO sheets is maintained during photocatalysis. Arguably, the rGO content would decrease since each photocatalytic cycle is followed by centrifugation and washing with water; thus, a rapid decrease in the photocatalytic performance after each cycle would be observed.

As presented above, the unmodified ZnO–TiO$_2$ core-shell photocatalyst exhibited a low, nonnegligible photoactivity in the visible light range. As mentioned in the experimental section, the lamp used in all photocatalytic experiments exhibited emission lines between 390 and 600 nm. The observed photoactivity of the ZnO–TiO$_2$ core-shell photocatalyst can be attributed to its band-gap value, which was measured as 3.08 eV (Table 1), corresponding to ~400 nm. Therefore, the ZnO–TiO$_2$ core-shell photocatalyst could be effectively activated in the 390–400 nm emission range of the lamp. The photocatalytic decoloration of MB by the ZT-rGO photocatalysts was significantly promoted compared to that of the parent core-shell photocatalyst. The observed superior performance of the ZT-rGO photocatalysts can be assigned to the rGO sheets acting as sensitizers in the visible

light, inducing band-gap narrowing and a shift in the absorption edge of the ZT-rGO materials toward the visible light range [49,50].
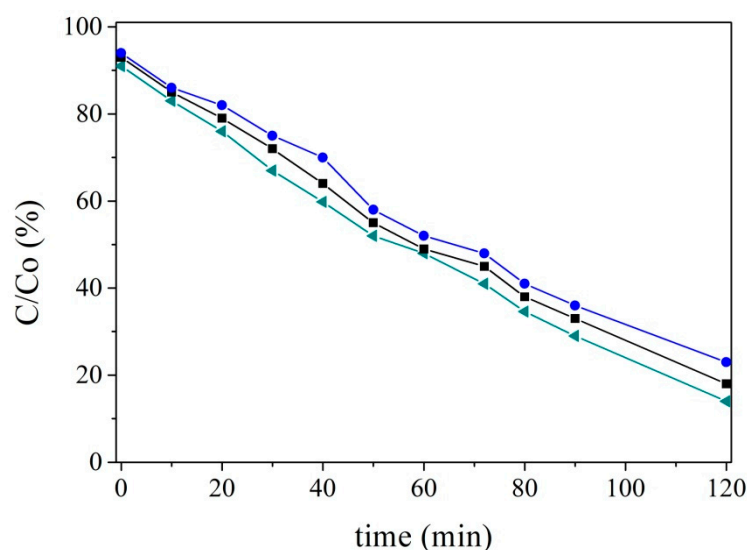
Figure 8. Decoloration of MB in the presence of the ZT-rGO catalyst with 2 wt % rGO for three photocatalytic cycles (cycle 1 ◄, cycle 2 ■ and cycle 3 ●).

The superior photocatalytic performance of the ZT-rGO core-shell architectures can also be attributed to the appropriate energy level differences between ZnO, TiO_2, and rGO. These differences result in a more efficient separation and migration of the photogenerated electrons and holes, significantly suppressing its recombination and promoting the photocatalytic rates. According to the literature, the conduction and valence bands of ZnO are more negatively charged (~0.48 eV) and are located above those of TiO_2 [1,17,51,52], while rGO has a work function of −4.42 eV [38,53–56]. Therefore, rGO can act as a trap for the electrons transferred to the conduction band of TiO_2 (−4.2 eV) from ZnO and hinder the charge recombination, which enhances the overall performance of the ternary photocatalyst [50,57,58]. However, a very high rGO loading (above the optimum value of 2 wt %) decreases the active sites on the surface of the photocatalyst, which become adversely blocked by the excessive rGO, resulting in the observed reduction of the photoactivity of the ternary photocatalyst [59,60].

To elucidate the radical species that are responsible for the photocatalytic removal of MB, radical trapping experiments were conducted by the addition of *tert*-butanol, (2,2,6,6-Tetramethylpiperidin-1-yl)oxyl (TEMPO), and ethylenediaminetetraacetic acid (EDTA) as ●OH, ●$O_2{}^-$, and h^+ traps, respectively, during the photocatalytic experiments (Figure 9).

The addition of EDTA, and thus the quenching of photogenerated holes, had an insignificant effect on the photocatalytic rates induced by the ZT-rGO photocatalyst with 2 wt % rGO. However, when quenching the OH radical with the alcohol, the MB removal efficiency decreased from 86% to 58% after 120 min of irradiation. This suggested that the highly reactive hydroxyl radicals produced by the photogenerated holes participate in the redox reactions. Moreover, an even more pronounced suppression of the photocatalytic performance (from 86% down to 40%) was observed upon scavenging the $O_2{}^-$ species with TEMPO, which indicated that the superoxide anion radicals were the main active species in the removal of MB, in agreement with the literature [16,19,61]. As discussed above, the modification of ZnO–TiO_2 with the rGO sheets increased the separation of electrons and holes, resulting in an increased migration of electrons on the graphene sheets, which reacted further with dissolved O_2 present in the reaction solution to generate the highly responsive $O_2{}^-$ species.
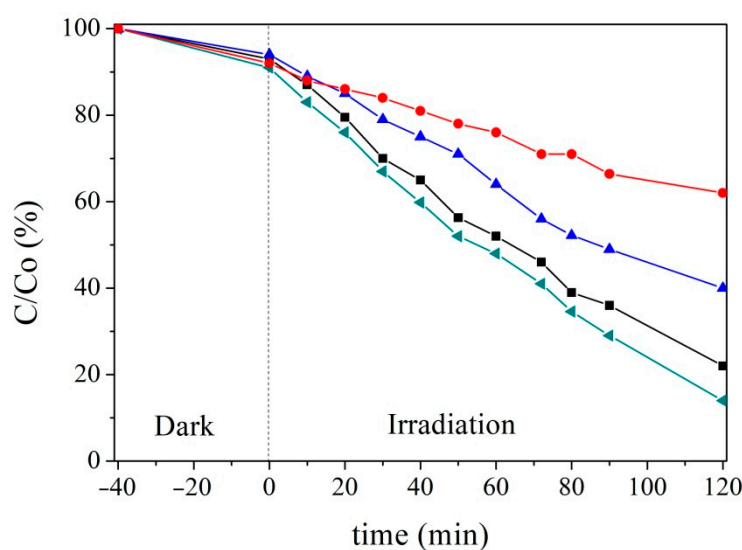
Figure 9. Decoloration of MB in the presence of ZT-rGO at 2 wt % rGO without scavenger (◄) and in the presence of 2,2,6,6-Tetramethylpiperidin-1-yl)oxyl (TEMPO) (●), ethylenediaminetetraacetic acid (EDTA) (■), and *tert*-butanol (▲) at 1.0 mM.

3. Materials and Methods

Zinc acetate dihydrate ($Zn(CH_3COO)_2 \cdot 2H_2O$, 99%), hydrochloric acid (HCl, 37 wt %), APTMS ($H_2N(CH_2)_3Si(OCH_3)_3$), sodium nitrate ($NaNO_3$), and graphite were supplied by Sigma Aldrich (St. Louis, Missouri United States); while MB (82%) and titanium isopropoxide ($Ti[OCH(CH_3)_2]_4$, 97%) were received from Aldrich. Potassium permanganate ($KMnO_4$) was obtained from Scharlau (Barcelona, Spain). Sulfuric acid (H_2SO_4) was purchased from PENTA (Prague, Czech Republic), while hydrogen peroxide (H_2O_2, 30% solution in H_2O) was provided by Chem-Lab. Ethanol (98%) was received from Honeywell (Charlotte, NC, USA) and was dried overnight over CaH_2 prior to use. Finally, Milli-Q water, obtained from a Millipore apparatus, with a resistivity of 18.2 $M\Omega \times$ cm at 298 K, was used for the preparation of all samples.

3.1. Synthesis of GO

For the synthesis of the GO, graphite powder (1.0 g) was first stirred into a mixture of H_2SO_4 (23 mL, 98%) and $NaNO_3$ (0.5 g) in an ice bath. Then, $KMnO_4$ (3 g) was slowly added over a period of 2 h. After 4 h, the reaction mixture was heated to 35 °C for 30 min and was added into H_2O (50 mL), followed by heating at 70 °C for 15 min. The mixture was then poured into 250 mL H_2O and the unreacted $KMnO_4$ was removed by the addition of 3% H_2O_2. The GO was purified by several centrifugation/redispersion cycles in H_2O and was dried under a vacuum overnight. An aqueous GO suspension (0.5 mg GO/mL H_2O) was prepared by ultrasonication for 1 h.

3.2. Synthesis of ZnO Flower-Like Structures and ZnO–TiO$_2$ Core-shell Heterostructures

The synthesis of the ZnO flower-like structures, as well as the ZnO-TiO$_2$ core-shell, flower-like heterostructures, has been described in detail in our previous work [2]. Briefly, ZnO, with a flower-like morphology, was prepared via the reaction of 40 mL of a 0.035 M $Zn(CH_3COO)_2 \cdot 2H_2O$ and 0.055 M NaOH aqueous solution at 70 °C for 24 h. For the synthesis of the ZnO-TiO$_2$ core-shell, flower-like heterostructures, 0.1 g ZnO flowers were first dispersed in 35 mL ethanol by ultrasonication. A solution of 0.25 mL $Ti[OCH(CH_3)_2]_4$ in 5 mL ethanol was prepared separately and was added dropwise in the ZnO dispersion. The dispersion was transferred in a preheated oil bath at 80 °C and a 10 mL mixture of water in ethanol (50 mL/L) was added via dropwise. After 2 h, the ZnO-TiO$_2$ core-shell catalyst was isolated by centrifugation, washed thoroughly with ethanol, and dried under a vacuum.

3.3. Synthesis of ZnO–TiO₂ Core-Shell Structures Wrapped with rGO

First, the ZnO–TiO₂ core-shell structures (400 mg) were ultrasonically dispersed in 200 mL dry ethanol. Then 3 mL APTMS was injected in the dispersion, followed by an overnight reflux at 90 °C. Finally, the APTMS-modified ZnO–TiO₂ flowers were rinsed thrice with ethanol and dried under a vacuum.

Next, 300 mg of the APTMS-modified ZnO–TiO₂ heterostructures were dispersed in 100 mL H_2O by ultrasonication, and an appropriate amount of the GO suspension was added under vigorous stirring to obtain ternary photocatalysts with 0.5, 2, and 5 wt % theoretical GO content. After stirring for 1 h, the GO-modified inorganic heterostructures were washed repeatedly with H_2O and dried under a vacuum. This process was repeated for the ternary photocatalyst with 2 wt % GO, using core-shell heterostructures without the APTMS functionalization to elucidate the effect of the amine groups on the interactions between the GO sheets and the inorganic core-shell structures.

To induce the reduction of GO to rGO, the GO-modified ZnO–TiO₂ flower-like particles were dispersed in a mixture of H_2O/EtOH (2:1) and were hydrothermally treated at 120 °C for 24 h in a Teflon-lined, stainless-steel autoclave. Finally, the ternary photocatalysts were calcined at 500 °C for 2 h under N_2, to further reduce rGO and crystallize TiO₂.

3.4. Characterization

The ternary core-shell structures were characterized by Raman spectroscopy using a Nicolet Almega XR Raman spectrometer (Thermo Scientific, Waltham, MA, USA) with a 473 nm blue laser as the excitation source in high resolution mode. ATR-FTIR spectra were recorded on a Thermo Scientific Nicolet 6700 spectrometer in the 400–4000 cm^{-1} range. We collected 64 scans at a resolution of 4 cm^{-1}. XRD patterns were measured on a PANalytical (Almelo, Netherlands) Xpert Pro X-ray diffractometer, using Cu-Kα radiation (45 kV and 40 mA). UV–Vis diffuse reflectance spectra in the 300–800 nm wavelength range were obtained using a Shimadzu UV-2401 PC spectrophotometer with an ISR-240A integrating sphere, with $BaSO_4$ powder used as a 100% reflectance standard. Finally, the morphology of the samples was investigated by field emission scanning electron microscopy (FE-SEM, JEOL JSM-7000F).

3.5. Photocatalytic Study

The photocatalytic performance of the parent and the rGO-modified ZnO–TiO₂ core-shell semiconductors was quantified via the decoloration of MB dye solutions (20 mg/L) under visible-light irradiation at pH 5 (corresponding to the natural pH of the solutions). The photocatalytic reactions were conducted at a photocatalyst loading of 160 ppm, while no catalyst was added for the photolytic experiments. The photocatalyst dispersion in the dye solutions was first stirred in the dark for ca. 40 min to establish the MB adsorption/desorption equilibrium, followed by irradiation using a medium-pressure mercury lamp emitting in the 200–600 nm range. The lamp was placed in a glass jacket that filtered out the UV lines at λ_{exc} < 390 nm (Table S1) [2,6]. All photocatalytic experiments were carried out in duplicate. To evaluate the reusability of the most photoactive photocatalyst, three photocatalytic cycles were conducted by recovering the catalyst after each cycle by centrifugation and washing thrice with H_2O before the next cycle.

4. Conclusions

In summary, complex ZnO–TiO₂ core-shell, flower-like structures wrapped with rGO sheets were prepared by a simple and well-controlled synthetic approach. First, core-shell flowers with a wurtzite ZnO core and an anatase TiO₂ shell of 59 ± 7 nm thickness were prepared and their surfaces were functionalized with primary amino groups using APTMS. The surface-modified ZnO–TiO₂ core-shell structures were then hydrothermally wrapped with rGO sheets at 0.5, 2, and 5 wt % loading. The amine functionalities on the inorganic surface induced strong adhesion of the rGO sheets on the TiO₂ shell due to favorable electrostatic interactions. The rGO-modified ZnO–TiO₂ photocatalysts exhibited superior

photoactivity in the decoloration of aqueous solutions of MB under visible-light irradiation compared with that of the parent ZnO–TiO$_2$ core-shell structures, which was dependent on the rGO loading. Specifically, the ternary photocatalyst with a 2 wt % rGO content resulted in ~86% dye removal after 120 min of irradiation, which was significantly higher than the ~51% decoloration found for the parent ZnO–TiO$_2$. Overall, the enhanced photocatalytic response of the ternary photocatalysts was attributed to the increase in the absorption in the visible-light range, as well as the promoted electron and hole separation due to the favorable energy level differences between ZnO, TiO$_2$, and rGO. Notably, excessive rGO loading above the optimum value of 2 wt % diminished the photoactivity of the ternary heterostructures to ~60% MB removal because of the decrease in free active sites on the surface of the photocatalyst.

Supplementary Materials: The following are available online at https://www.mdpi.com/2073-4344/11/3/332/s1, Figure S1. Higher magnification SEM images of the (a) bare ZnO flowers, (b) ZnO-TiO$_2$ core-shell heterostructures, and (c) ZT-rGO structures at a 2 wt % rGO loading, Table S1. Radiation flux Φ for the immersion lamp used in this study, Figure S2. Decoloration of MB in the absence of a photocatalyst (●) and in the presence of the parent ZnO–TiO$_2$ core-shell flowers (■), and ZT-rGO at 0.5 wt % (♦), 2 wt % (◄), and 5 wt % (▲) rGO. All values were corrected for the adsorption component.

Conflicts of Interest: The authors declare no conflict of interest.

References

1. Kwiatkowski, M.; Bezverkhyy, I.; Skompska, M. ZnO nanorods covered with a TiO$_2$ layer: Simple sol–gel preparation, and optical, photocatalytic and photoelectrochemical properties. *J. Mater. Chem. A* **2015**, *3*, 12748–12760. [CrossRef]
2. Vasilaki, E.; Vamvakaki, M.; Katsarakis, N. Complex ZnO-TiO$_2$ Core–Shell Flower-Like Architectures with Enhanced Photocatalytic Performance and Superhydrophilicity without UV Irradiation. *Langmuir* **2018**, *34*, 9122–9132. [CrossRef] [PubMed]
3. Boyadjiev, S.I.; Kéri, O.; Bárdos, P.; Firkala, T.; Gáber, F.; Nagy, Z.K.; Baji, Z.; Takács, M.; Szilágyi, I.M. TiO$_2$/ZnO and ZnO/TiO$_2$ core/shell nanofibers prepared by electrospinning and atomic layer deposition for photocatalysis and gas sensing. *Appl. Surf. Sci.* **2017**, *424*, 190–197. [CrossRef]
4. Pan, L.; Shen, G.-Q.; Zhang, J.-W.; Wei, X.-C.; Wang, L.; Zou, J.-J.; Zhang, X. TiO$_2$–ZnO Composite Sphere Decorated with ZnO Clusters for Effective Charge Isolation in Photocatalysis. *Ind. Eng. Chem. Res.* **2015**, *54*, 7226–7232. [CrossRef]
5. Chu, Y.-M.; Javed, H.M.; Awais, M.; Khan, M.I.; Shafqat, S.; Khan, F.S.; Mustafa, M.S.; Ahmed, D.; Khan, S.U.; Khalil, R.M. Photocatalytic Pretreatment of Commercial Lignin Using TiO$_2$-ZnO Nanocomposite-Derived Advanced Oxidation Processes for Methane Production Synergy in Lab Scale Continuous Reactors. *Catalysts* **2021**, *11*, 54. [CrossRef]
6. Vasilaki, E.; Georgaki, I.; Vernardou, D.; Vamvakaki, M.; Katsarakis, N. Ag-loaded TiO$_2$/reduced graphene oxide nanocomposites for enhanced visible-light photocatalytic activity. *Appl. Surf. Sci.* **2015**, *353*, 865–872. [CrossRef]
7. Lv, W.; Wei, B.; Xu, L.; Zhao, Y.; Gao, H.; Liu, J. Photocatalytic properties of hierarchical ZnO flowers synthesized by a sucrose-assisted hydrothermal method. *Appl. Surf. Sci.* **2012**, *259*, 557–561. [CrossRef]
8. Qin, J.; Zhang, X.; Yang, C.; Cao, M.; Ma, M.; Liu, R. ZnO microspheres-reduced graphene oxide nanocomposite for photocatalytic degradation of methylene blue dye. *Appl. Surf. Sci.* **2017**, *392*, 196–203. [CrossRef]
9. Zhang, B.; Yang, F.; Liu, H.; Yan, L.; Yang, W.; Xu, C.; Huang, S.; Li, Q.; Bao, W.; Liu, B.; et al. Assembling Graphene-Encapsulated Pd/TiO$_2$ Nanosphere with Hierarchical Architecture for High-Performance Visible-Light-Assisted Methanol Electro-Oxidation Material. *Ind. Eng. Chem. Res.* **2019**, *58*, 19486–19494. [CrossRef]

10. Sookhakian, M.; Amin, Y.M.; Zakaria, R.; Baradaran, S.; Mahmoudian, M.R.; Rezayi, M.; Tajabadi, M.T.; Basirun, W.J. Enhanced Photovoltaic Performance of Polymer Hybrid Nanostructure Heterojunction Solar Cells Based on Poly(3-hexylthiophene)/ZnS/ZnO/Reduced Graphene Oxide Shell–Core Nanorod Arrays. *Ind. Eng. Chem. Res.* **2014**, *53*, 14301–14309. [CrossRef]

11. Ong, W.-J.; Voon, S.-Y.; Tan, L.-L.; Goh, B.T.; Yong, S.-T.; Chai, S.-P. Enhanced Daylight-Induced Photocatalytic Activity of Solvent Exfoliated Graphene (SEG)/ZnO Hybrid Nanocomposites toward Degradation of Reactive Black 5. *Ind. Eng. Chem. Res.* **2014**, *53*, 17333–17344. [CrossRef]

12. Johra, F.T.; Jung, W.-G. RGO–TiO_2–ZnO composites: Synthesis, characterization, and application to photocatalysis. *Appl. Catal. A Gen.* **2015**, *491*, 52–57. [CrossRef]

13. Potle, V.D.; Shirsath, S.R.; Bhanvase, B.A.; Saharan, V.K. Sonochemical preparation of ternary rGO-ZnO-TiO_2 nanocomposite photocatalyst for efficient degradation of crystal violet dye. *Optik* **2020**, *208*, 164555. [CrossRef]

14. Liu, X.; Pan, L.; Lv, T.; Sun, Z. Investigation of photocatalytic activities over ZnO–TiO_2–reduced graphene oxide composites synthesized via microwave-assisted reaction. *J. Colloid Interface Sci.* **2013**, *394*, 441–444. [CrossRef]

15. Raghavan, N.; Thangavel, S.; Venugopal, G. Enhanced photocatalytic degradation of methylene blue by reduced graphene-oxide/titanium dioxide/zinc oxide ternary nanocomposites. *Mater. Sci. Semicond. Process.* **2015**, *30*, 321–329. [CrossRef]

16. Divya, K.S.; Xavier, M.M.; Vandana, P.V.; Reethu, V.N.; Mathew, S. A quaternary TiO_2/ZnO/RGO/Ag nanocomposite with enhanced visible light photocatalytic performance. *New J. Chem.* **2017**, *41*, 6445–6454. [CrossRef]

17. Malekshoar, G.; Pal, K.; He, Q.; Yu, A.; Ray, A.K. Enhanced Solar Photocatalytic Degradation of Phenol with Coupled Graphene-Based Titanium Dioxide and Zinc Oxide. *Ind. Eng. Chem. Res.* **2014**, *53*, 18824–18832. [CrossRef]

18. Van Bao, H.; Dat, N.M.; Giang, N.T.H.; Thinh, D.B.; Tai, L.T.; Trinh, D.N.; Hai, N.D.; Khoa, N.A.D.; Huong, L.M.; Nam, H.M.; et al. Behavior of ZnO-doped TiO_2/rGO nanocomposite for water treatment enhancement. *Surf. Interfaces* **2021**, *23*, 100950. [CrossRef]

19. Nguyen, C.H.; Tran, M.L.; Van Tran, T.T.; Juang, R.-S. Enhanced removal of various dyes from aqueous solutions by UV and simulated solar photocatalysis over TiO_2/ZnO/rGO composites. *Sep. Purif. Technol.* **2020**, *232*, 115962. [CrossRef]

20. Pan, X.; Yang, P.; Nan, H.; Yang, L.; Chen, H.; Zhao, X. Preparation and enhanced visible-light photoelectrocatalytic activity of ternary TiO_2ZnO/RGO nanocomposites. *Electrochim. Acta* **2018**, *261*, 284–288. [CrossRef]

21. Li, Q.; Li, X.; Swelm, W.; Al-Ghamdi, A.A.; Yu, J. CdS/Graphene Nanocomposite Photocatalysts. *Adv. Energy Mater.* **2015**, *5*, 1500010. [CrossRef]

22. Liang, Y.; Wang, H.; Casalongue, H.S.; Chen, Z.; Dai, H. TiO_2 nanocrystals grown on graphene as advanced photocatalytic hybrid materials. *Nano Res.* **2010**, *3*, 701–705. [CrossRef]

23. Pei, F.; Xu, S.; Zuo, W.; Zhang, Z.; Liu, Y.; Cao, S. Effective improvement of photocatalytic hydrogen evolution via a facile in-situ solvothermal N-doping strategy in N-TiO_2/N-graphene nanocomposite. *Int. J. Hydrogen Energy* **2014**, *39*, 6845–6852. [CrossRef]

24. Cao, X.; Tian, G.; Chen, Y.; Zhou, J.; Zhou, W.; Tian, C.; Fu, H. Hierarchical composites of TiO_2 nanowire arrays on reduced graphene oxide nanosheets with enhanced photocatalytic hydrogen evolution performance. *J. Mater. Chem. A* **2014**, *2*, 4366–4374. [CrossRef]

25. Shen, J.; Shi, M.; Yan, B.; Ma, H.; Li, N.; Ye, M. Ionic liquid-assisted one-step hydrothermal synthesis of TiO_2-reduced graphene oxide composites. *Nano Res.* **2011**, *4*, 795–806. [CrossRef]

26. Poh, H.L.; Šaněk, F.; Ambrosi, A.; Zhao, G.; Sofer, Z.; Pumera, M. Graphenes prepared by Staudenmaier, Hofmann and Hummers methods with consequent thermal exfoliation exhibit very different electrochemical properties. *Nanoscale* **2012**, *4*, 3515–3522. [CrossRef]

27. Johra, F.T.; Lee, J.-W.; Jung, W.-G. Facile and safe graphene preparation on solution based platform. *J. Ind. Eng. Chem.* **2014**, *20*, 2883–2887. [CrossRef]

28. Stobinski, L.; Lesiak, B.; Malolepszy, A.; Mazurkiewicz, M.; Mierzwa, B.; Zemek, J.; Jiricek, P.; Bieloshapka, I. Graphene oxide and reduced graphene oxide studied by the XRD, TEM and electron spectroscopy methods. *J. Electron. Spectrosc. Relat. Phenom.* **2014**, *195*, 145–154. [CrossRef]

29. Zhang, K.; Zhang, Y.; Wang, S. Enhancing thermoelectric properties of organic composites through hierarchical nanostructures. *Sci. Rep.* **2013**, *3*, 3448. [CrossRef] [PubMed]

30. Kudin, K.N.; Ozbas, B.; Schniepp, H.C.; Prud'Homme, R.K.; Aksay, I.A.; Car, R. Raman Spectra of Graphite Oxide and Functionalized Graphene Sheets. *Nano Lett.* **2008**, *8*, 36–41. [CrossRef]

31. Kim, H.J.; Lee, S.-M.; Oh, Y.-S.; Yang, Y.-H.; Lim, Y.S.; Yoon, D.H.; Lee, C.; Kim, J.-Y.; Ruoff, R.S. Unoxidized Graphene/Alumina Nanocomposite: Fracture- and Wear-Resistance Effects of Graphene on Alumina Matrix. *Sci. Rep.* **2015**, *4*, 5176. [CrossRef] [PubMed]

32. Wang, Y.; Li, Y.; Tang, L.; Lu, J.; Li, J. Application of graphene-modified electrode for selective detection of dopamine. *Electrochem. Commun.* **2009**, *11*, 889–892. [CrossRef]

33. Shen, J.; Yan, B.; Shi, M.; Ma, H.; Li, N.; Ye, M. One step hydrothermal synthesis of TiO_2-reduced graphene oxide sheets. *J. Mater. Chem.* **2011**, *21*, 3415–3421. [CrossRef]

34. Tan, L.-L.; Ong, W.-J.; Chai, S.-P.; Mohamed, A.R. Reduced graphene oxide-TiO_2 nanocomposite as a promising visible-light-active photocatalyst for the conversion of carbon dioxide. *Nanoscale Res. Lett.* **2013**, *8*, 465. [CrossRef] [PubMed]

35. Zhang, J.; Xiao, F.-X.; Xiao, G.; Liu, B. Self-assembly of a Ag nanoparticle-modified and graphene-wrapped TiO_2 nanobelt ternary heterostructure: Surface charge tuning toward efficient photocatalysis. *Nanoscale* **2014**, *6*, 11293–11302. [CrossRef] [PubMed]

36. Yang, X.; Chen, W.; Huang, J.; Zhou, Y.; Zhu, Y.; Li, C. Rapid degradation of methylene blue in a novel heterogeneous Fe_3O_4 @rGO@TiO$_2$-catalyzed photo-Fenton system. *Sci. Rep.* **2015**, *5*, 10632. [CrossRef]

37. Zheng, P.; Liu, T.; Su, Y.; Zhang, L.; Guo, S. TiO$_2$ nanotubes wrapped with reduced graphene oxide as a high-performance anode material for lithium-ion batteries. *Sci. Rep.* **2016**, *6*, 36580. [CrossRef]

38. Lee, J.S.; You, K.H.; Park, C.B. Highly Photoactive, Low Bandgap TiO$_2$ Nanoparticles Wrapped by Graphene. *Adv. Mater.* **2012**, *24*, 1084–1088. [CrossRef] [PubMed]

39. Lui, G.; Liao, J.-Y.; Duan, A.; Zhang, Z.; Fowler, M.; Yu, A. Graphene-wrapped hierarchical TiO$_2$ nanoflower composites with enhanced photocatalytic performance. *J. Mater. Chem. A* **2013**, *1*, 12255–12262. [CrossRef]

40. Liu, C.; Hao, F.; Zhao, X.; Zhao, Q.; Luo, S.; Lin, H. Low temperature reduction of free-standing graphene oxide papers with metal iodides for ultrahigh bulk conductivity. *Sci. Rep.* **2015**, *4*, 1–6. [CrossRef] [PubMed]

41. Shu, W.; Liu, Y.; Peng, Z.; Chen, K.; Zhang, C.; Chen, W. Synthesis and photovoltaic performance of reduced graphene oxide–TiO$_2$ nanoparticles composites by solvothermal method. *J. Alloys Compd.* **2013**, *563*, 229–233. [CrossRef]

42. Ngo-Duc, T.; Singh, K.; Meyyappan, M.; Oye, M.M. Vertical ZnO nanowire growth on metal substrates. *Nanotechnology* **2012**, *23*, 194015. [CrossRef] [PubMed]

43. Zhang, R.; Yin, P.-G.; Wang, N.; Guo, L. Photoluminescence and Raman scattering of ZnO nanorods. *Solid State Sci.* **2009**, *11*, 865–869. [CrossRef]

44. Singh, A.K.; Thool, G.S.; Bangal, P.R.; Madhavendra, S.S.; Singh, S.P. Low Temperature Mn Doped ZnO Nanorod Array: Synthesis and Its Photoluminescence Behavior. *Ind. Eng. Chem. Res.* **2014**, *53*, 9383–9390. [CrossRef]

45. Min, Y.; Zhang, K.; Zhao, W.; Zheng, F.; Chen, Y.; Zhang, Y. Enhanced chemical interaction between TiO$_2$ and graphene oxide for photocatalytic decolorization of methylene blue. *Chem. Eng. J.* **2012**, *193–194*, 203–210. [CrossRef]

46. Zhang, H.; Lv, X.; Li, Y.; Wang, Y.; Li, J. P25-Graphene Composite as a High Performance Photocatalyst. *ACS Nano* **2009**, *4*, 380–386. [CrossRef]

47. Sakthivel, S.; Kisch, H. Daylight Photocatalysis by Carbon-Modified Titanium Dioxide. *Angew. Chem. Int. Ed.* **2003**, *42*, 4908–4911. [CrossRef] [PubMed]

48. Kwiatkowski, M.; Chassagnon, R.; Heintz, O.; Geoffroy, N.; Skompska, M.; Bezverkhyy, I. Improvement of photocatalytic and photoelectrochemical activity of ZnO/TiO$_2$ core/shell system through additional calcination: Insight into the mechanism. *Appl. Catal. B Environ.* **2017**, *204*, 200–208. [CrossRef]

49. Nguyen-Phan, T.-D.; Pham, V.H.; Shin, E.W.; Pham, H.-D.; Kim, S.; Chung, J.S.; Kim, E.J.; Hur, S.H. The role of graphene oxide content on the adsorption-enhanced photocatalysis of titanium dioxide/graphene oxide composites. *Chem. Eng. J.* **2011**, *170*, 226–232. [CrossRef]

50. Chen, C.; Cai, W.; Long, M.; Zhou, B.; Wu, Y.; Wu, D.; Feng, Y. Synthesis of Visible-Light Responsive Graphene Oxide/TiO$_2$ Composites with p/n Heterojunction. *ACS Nano* **2010**, *4*, 6425–6432. [CrossRef] [PubMed]

51. Scanlon, D.O.; Dunnill, C.W.; Buckeridge, J.; Shevlin, S.A.; Logsdail, A.J.; Woodley, S.M.; Catlow, C.R.A.; Powell, M.J.; Palgrave, R.G.; Parkin, I.P.; et al. Band alignment of rutile and anatase TiO$_2$. *Nat. Mater.* **2013**, *12*, 798–801. [CrossRef]

52. Lei, Y.; Zhao, G.; Liu, M.; Zhang, Z.; Tong, X.; Cao, T. Fabrication, Characterization, and Photoelectrocatalytic Application of ZnO Nanorods Grafted on Vertically Aligned TiO$_2$ Nanotubes. *J. Phys. Chem. C* **2009**, *113*, 19067–19076. [CrossRef]

53. Zhang, J.; Xiong, Z.; Zhao, X.S. Graphene–metal–oxide composites for the degradation of dyes under visible light irradiation. *J. Mater. Chem.* **2011**, *21*, 3634–3640. [CrossRef]

54. Liu, L.; Bai, H.; Liu, J.; Sun, D.D. Multifunctional graphene oxide-TiO$_2$-Ag nanocomposites for high performance water disinfection and decontamination under solar irradiation. *J. Hazard. Mater.* **2013**, *261*, 214–223. [CrossRef] [PubMed]

55. Wang, P.; Wang, J.; Ming, T.; Wang, X.; Yu, H.; Yu, J.; Wang, Y.; Lei, M. Dye-Sensitization-Induced Visible-Light Reduction of Graphene Oxide for the Enhanced TiO$_2$ Photocatalytic Performance. *ACS Appl. Mater. Interfaces* **2013**, *5*, 2924–2929. [CrossRef]

56. Wei, L.; Chen, S.; Yang, Y.; Dong, Y.; Song, W.; Fan, R. Reduced graphene oxide modified TiO$_2$ semiconductor materials for dye-sensitized solar cells. *RSC Adv.* **2016**, *6*, 100866–100875. [CrossRef]

57. Shang, Q.; Huang, X.; Tan, X.; Yu, T. High Activity Ti^{3+}-Modified Brookite TiO$_2$/Graphene Nanocomposites with Specific Facets Exposed for Water Splitting. *Ind. Eng. Chem. Res.* **2017**, *56*, 9098–9106. [CrossRef]

58. Huang, Y.; Li, R.; Chen, D.; Hu, X.; Chen, P.; Chen, Z.; Li, D. Synthesis and Characterization of CNT/TiO$_2$/ZnO Composites with High Photocatalytic Performance. *Catalysts* **2018**, *8*, 151. [CrossRef]

59. Zhang, Y.; Tang, Z.-R.; Fu, X.; Xu, Y.-J. TiO$_2$−Graphene Nanocomposites for Gas-Phase Photocatalytic Degradation of Volatile Aromatic Pollutant: Is TiO$_2$−Graphene Truly Different from Other TiO$_2$−Carbon Composite Materials? *ACS Nano* **2010**, *4*, 7303–7314. [CrossRef] [PubMed]

60. Zhou, K.; Zhu, Y.; Yang, X.; Jiang, X.; Li, C. Preparation of graphene–TiO$_2$ composites with enhanced photocatalytic activity. *New J. Chem.* **2011**, *35*, 353–359. [CrossRef]

61. Simsek, E.B.; Kilic, B.; Asgin, M.; Akan, A. Graphene oxide based heterojunction TiO$_2$ –ZnO catalysts with outstanding photocatalytic performance for bisphenol-A, ibuprofen and flurbiprofen. *J. Ind. Eng. Chem.* **2018**, *59*, 115–126. [CrossRef]